

Signatures and mechanisms of efficacious therapeutic ribonucleotides against SARS-CoV-2 revealed by analysis of its replicase using magnetic tweezers

Mona Seifert^{1, †}, Subhas Chandra Bera^{1, †}, Pauline van Nies¹, Robert N. Kirchdoerfer², Ashleigh Shannon³, Thi-Tuyet-Nhung Le³, Tyler L. Grove⁴, Flávia S. Papini¹, Jamie J. Arnold⁵, Steven C. Almo⁴, Bruno Canard³, Martin Depken⁶, Craig E. Cameron⁵, and David Dulin^{1,*}

- 1 Junior Research Group 2, Interdisciplinary Center for Clinical Research, Friedrich-Alexander-University Erlangen-Nürnberg (FAU), Cauerstr. 3, 91058 Erlangen, Germany
- 2 Department of Biochemistry and Institute of Molecular Virology, University of Wisconsin-Madison, Madison, WI 53706
- 3 Architecture et Fonction des Macromolécules Biologiques, CNRS and Aix-Marseille Université, UMR 7257, Polytech Case 925, 13009 Marseille, France.
- 4 Department of Biochemistry, Albert Einstein College of Medicine, Bronx, NY, USA
Institute for Protein Innovation, Boston, MA, USA
- 5 Department of Microbiology and Immunology, University of North Carolina School of Medicine, Chapel Hill, NC 27514 USA
- 6 Department of Bionanoscience, Kavli Institute of Nanoscience, Delft University of Technology, Van der Maasweg 9, 2629 HZ Delft, The Netherlands

† These authors contributed equally to this work.

*Corresponding author: Email: david.dulin@uk-erlangen.de

Summary

Coronavirus Disease 2019 (COVID-19) results from an infection by the severe acute respiratory syndrome coronavirus 2 (SARS-CoV-2), the third coronavirus outbreak to plague humanity this century. Currently, the most efficacious therapeutic against SARS-CoV-2 infection is the Remdesivir (RDV), an adenine-like ribonucleotide analogue that is very efficiently incorporated by the SARS-CoV-2 replicase. Understanding why RDV is so well incorporated will facilitate development of even more effective therapeutics. Here, we have applied a high-throughput, single-molecule, magnetic-tweezers platform to study thousands of cycles of nucleotide addition by the SARS-CoV-2 replicase in the absence and presence of RDV, a Favipiravir-related analog (T-1106), and the endogenously produced ddhCTP. Our data are consistent with two parallel catalytic pathways of the replicase: a high-fidelity catalytic (HFC) state and a low-fidelity catalytic (LFC) state, the latter allowing the slow incorporation of both cognate and non-cognate nucleotides. ddhCTP accesses HFC, T-1106 accesses LFC as a non-cognate nucleotide, while RDV efficiently accesses both LFC pathway. In contrast to previous reports, we provide unequivocal evidence against RDV functioning as a chain terminator. We show that RDV incorporation transiently stalls the replicase, only appearing as termination events when traditional, gel-based assays are used. The efficiency of ddhCTP utilization by the SARS-CoV-2 replicase suggests suppression of its synthesis during infection, inspiring new therapeutic strategies. Use of this experimental paradigm will be essential to the development of therapeutic nucleotide analogs targeting polymerases.

Introduction

SARS-CoV-2 has infected almost twenty million humans worldwide, causing approximately 700,000 deaths as August 5th, with numbers still on the rise. We are currently living through the third coronavirus outbreak in less than twenty years, and we are desperately in need of broad-spectrum antiviral drugs that are capable of targeting this emerging family of human pathogens. To this end, nucleotide analogues (NAs) represent a powerful approach, as they target the functionally and structurally conserved coronavirus replicase, and their insertion in the viral RNA induces either premature termination or a lethal increase in mutations. The coronavirus replicase is composed of the RNA-dependent RNA polymerase (RdRp) nsp12, and the nsp7 and nsp8 co-factors, with a stoichiometry of 1:1:2¹⁻⁴. This core replicase associates with several additional viral proteins, including the 5'-to-3' helicase nsp13⁵ and the 3'-to-5' exonuclease nsp14⁶⁻¹¹. The latter proofreads the RNA synthesized by the high error prone RdRp nsp12¹², a unique feature of coronavirus in the RNA virus world, and therefore plays a

central role in contributing to the stability of the unusually large coronavirus genome, i.e. ~30 kb. Furthermore, nsp14 confers coronavirus resistance against many established NAs (e.g., ribavirin¹³) and therefore presents a challenge for the development of potent NAs. Remdesivir (RDV) is a recently discovered NA that showed efficacy against Ebola infection¹⁴, and has been successfully repurposed for the treatment of coronavirus infection^{6,15-19}. The success of RDV relies on its efficient incorporation by nsp12¹⁶, and probable evasion from excision by nsp14⁶. Understanding how RDV achieves these two tasks will help to guide the rational design of more efficacious NAs for the current and future outbreaks. To this end, it is essential to build a comprehensive model describing the selection and incorporation mechanisms that control the utilization of NAs by coronavirus replicase and to define the determinants of the base and ribose responsible for selectivity and potency. The generation of such model is however hampered by the inability of standard biochemical techniques to work in physiological conditions involving saturating concentrations of competing NTP and kilobase-long template, while maintaining single base resolution.

Results

Monitoring SARS-CoV-2 replication at the single molecule level

To enable the observation of rare events, such as nucleotide mismatch and NA incorporation, even in the presence of saturating NTP concentration, we have developed a single molecule, high throughput, magnetic tweezers assay to monitor SARS-CoV-2 replication activity at near single base resolution²⁰. A SARS-CoV-2 replicase formed of nsp12, nsp7 and nsp8 assembles and initiates replication at the 3' end of the magnetic bead-attached handle, and converts the 1043 nt long single stranded RNA template into a double-stranded (ds) RNA in the presence of NTPs (**Fig. 1a, Extended data Fig. 1ab, Materials and Methods**). The magnetic bead displacement along the vertical axis directly informs on the number of incorporated nucleotides (**Fig. 1a, Materials and Methods**)²¹. During each experiment, hundreds of magnetic beads are followed in parallel (**Extended data Fig. 1c**), providing dozens of SARS-CoV-2 replication activity traces per experiment (**Fig. 1b**). As previously observed for other viral RdRps²⁰⁻²², the traces present a lot of dynamics, with bursts of activity interrupted by pauses of duration varying from ~0.5 s to ~60 s in **Fig. 1b**. To extract the elongation kinetics of SARS-CoV-2 replicase, we scanned the traces with non-overlapping windows of 10 nt to measure the ten successive nucleotide incorporations total duration, which we coined dwell time²⁰⁻²² (**Materials and Methods**). We fitted the distribution of dwell times using the stochastic-pausing model that describes well the fidelity and kinetics of nucleotide addition of viral RdRps²⁰⁻²³ (**Fig. 1c,**

Materials and Methods), and in particular for poliovirus RdRp, a prototypical enterovirus RdRp to which SARS-CoV-1 nsp12 resembles the most¹. This model is composed of four distributions, describing the pause-free nucleotide addition rate, Pause 1, Pause 2 and the long-lived pauses (**Fig. 1c**). Statistics and all parameter values extracted from the analysis are reported in **Extended data Table 1**. Viral RdRps, such as the one of poliovirus, are robustly described by a kinetic model where the nucleotide addition rate is the kinetic signature of a fast and high fidelity catalytic (HFC) state, from which the RdRp stochastically and rarely switches into a lower fidelity catalytic (LFC) state that runs parallel to the HFC state (**Fig. 1d**)²⁰⁻²². Pause 1 and Pause 2 are the kinetic signatures of the LFC state, and relate to the slow incorporation of a cognate base following either a cognate, i.e. diagonal arrow in **Fig. 1d**, or a mismatch base incorporation, i.e. terminal mismatch catalytic state (TMC) in **Fig. 1d**, respectively. On the other hand, the long-lived pauses relate to a catalytically incompetent state²¹. Increasing the temperature from 25°C to 37°C, SARS-CoV-2 replicase reveals a strong temperature dependence, which translates into a 2-fold decrease in median of the total replication time, from $(25 \pm 1) s$ to $(12.0 \pm 0.4) s$ (median \pm standard deviation (**Fig. 1e**)), while not affecting the replication product length (**Fig. 1f**). Analyzing the dwell time distribution at 25 and 37°C (**Fig. 1g**), we extracted a ~ 2.6 -fold enhancement in nucleotide addition rate, i.e. from $(65.6 \pm 0.5) s^{-1}$ to $(169 \pm 4) s^{-1}$, making nsp12 the fastest RNA polymerase characterized to date (**Fig. 1h**). Pause 1 and Pause 2 exit rates also increased by ~ 2 -fold (**Fig. 1h**), whereas their respective probabilities increased by 2- and 5-fold (**Extended data Fig. 1d**). The latter results are rather surprising, as enterovirus RdRps showed only an exit rate increase with no change in probability²².

3'-dATP versus Remdesivir-TP: two ATP competitors, two modes of incorporation

Next, we investigated how the elongation kinetics and the product length of SARS-CoV-2 replicase were affected by two adenosine analogues, i.e. 3'-dATP and RDV-TP (**Extended data Fig. 2**). 3'-dATP is an obligatory terminator and a recent study showed that dideoxynucleotides were incorporated by SARS-CoV-1 replicase⁸. In the presence of 500 μM NTP and 500 μM 3'-dATP, SARS-CoV-2 replication demonstrated an increase in the number of traces that did not reach the end of the template (1043 nt) (**Fig. 2a** versus **Fig. 1b**). Indeed, increasing 3'-dATP concentration up to 2000 μM , i.e. a stoichiometry equal to four, reduced the mean product length of SARS-CoV-2 replicase by ~ 1.7 -fold, i.e. from $(940 \pm 13) nt$ to $(566 \pm 33) nt$ (mean \pm standard deviation) (**Fig. 2b**), while neither affected the replication time nor the elongation kinetics (**Fig. 2c**, **Extended data Fig. 3abc**). We derived a model to

determine the effective incorporation rate γ of a NA chain terminator against an equimolar concentration of the competing nucleotide, i.e. a stoichiometry of 1 (**Materials and Methods**). This model fits very well the mean product length as a function of 3'-dATP stoichiometry against ATP (**Fig. 2b**), i.e. $\gamma_{3'-dATP,500 \mu M ATP} = (780 \pm 64) nt$, meaning that the replicase incorporates on average 780 nt before incorporating one 3'-dATP and terminating replication (**Materials and Methods**). A subsaturating concentration of NTP increases the probability to enter the LFC state (**Fig. 1d**)^{20,21}, i.e. Pause 1 and Pause 2 probability, and would increase the effective incorporation rate of 3'-dATP, providing it is incorporated via the LFC state. Decreasing ATP concentration from 500 to 50 μM , we observed an increase in Pause 1 and Pause 2 probabilities by more than 2-fold and 3-fold, i.e. from (0.060 ± 0.002) to (0.149 ± 0.005) and from (0.0033 ± 0.0009) to (0.0115 ± 0.0026) , respectively (**Extended data Fig. 3a-f**), respectively, and the replication traces appeared shorter than at 500 μM ATP (**Fig. 2d**). However, the effective incorporation rate of 3'-dATP was identical at both concentrations of ATP, i.e. $\gamma_{3'-dATP,50 \mu M ATP} = (777 \pm 50) nt$ (**Fig. 2e**), which indicates that 3'-dATP incorporation is only driven by stoichiometry, despite the significant increase in the LFC state probabilities (Pause 1 and Pause 2). Therefore, we conclude that 3'-dATP is incorporated through the HFC state (**Fig. 1d**). This interpretation is further supported by steady state kinetics analysis of 3'-dATP incorporation by poliovirus RdRp, which showed that 3'-dATP is much more promiscuous than any mismatch on a uracil²⁴. Of note, the decrease in the median replication time is due to the shortening of the product length from early termination (**Extended data Fig. 3g**). Despite its good incorporation rate, 3'-dATP is not a good candidate to treat coronavirus infection, because of its toxicity²⁵. Therefore, a less toxic and promiscuous NA is required to compete against ATP. RDV-TP is an adenine analogue with a 1'-cyano modification that has recently been shown to outcompete ATP for incorporation¹⁶, while having a low cytotoxicity²⁶. RDV-TP has been proposed to induce delayed chain termination at i+3 (i being RDV incorporation position) during coronavirus replication^{15,16}. Adding 100 μM RDV-TP in a reaction buffer containing 500 μM NTPs showed a dramatic increase in the pause density and duration, while most of the traces reached the end of the template (**Fig. 2f**). We indeed observed a final product length largely unaffected at all concentrations of RDV-TP (**Fig. 2g**), while the median replication time increased by more than 10-fold, i.e. from $(25 \pm 1) s$ to $(315 \pm 14) s$ (**Fig. 2h**) for RDV-TP concentration increasing up to 300 μM . Therefore, the RDV-TP mechanism of action is not termination. We then investigated the origin of the pause induced by RDV-TP incorporation using our pause-stochastic model (**Fig. 2i**, **Extended data Fig. 4a**). While the nucleotide addition rate is unaffected by RDV-TP, all

pauses are significantly impacted. The exit rates of Pause 1 and Pause 2 decreased by 4- and 10-fold (**Fig. 2j**), while their probabilities increased by 2- and 4-fold, respectively (**Fig. 2k**). Most notably, the long-lived pause probability increased by 28-fold, i.e. from (0.0005 ± 0.0001) to (0.0142 ± 0.0015) when increasing RDV-TP concentration up to 300 μM . The long-lived pause probability increase was such that it most likely affected the probability and the exit rates of Pause 1 and Pause 2 above 50 μM RDV-TP (**Fig. 2k**). To better disentangle the pause distributions, we performed a SARS-CoV-2 replication experiments at 37°C with 100 μM RDV-TP (**Extended data Fig. 4b**). We observed the same nucleotide addition rate with and without RDV-TP (**Fig. 1bef**), while Pause 1 and Pause 2 exit rates significantly decreased by 3- and 9-fold, respectively (**Extended data Fig. 4c**). On the other hand, Pause 1 and Pause 2 probabilities were unaffected by the presence of RDV-TP (**Extended data Fig. 4d**), supporting the notion that the increase in probability in the experiments performed at 25°C was the consequence of the long-lived pauses biasing Pause 1 and Pause 2 distributions²⁰. The long-lived pause probability increased by more than 7-fold, i.e. from (0.0003 ± 0.0001) to (0.0022 ± 0.0007) . As RDV-TP incorporation pauses SARS-CoV-2 replicase, incorporation via the HFC state would increase a probability of Pause 1 and Pause 2. Here, we observed constant probabilities for Pause 1 and Pause 2, while their respective exit rates decreased, suggesting that RDV-TP is incorporated through the LFC state, behaving like a cognate (diagonal arrow in **Fig. 1d**) and as a non-cognate base (TMC, **Fig. 1d**), i.e. not opposite uracil. As expected, the almost identical SARS-CoV-1 replicase¹ demonstrated a similar kinetic signature to RDV-TP incorporation (**Extended data Fig. 5a-f, Table 1**), though to a lesser extent, e.g. the long-lived pause probability increased by ~9-fold when raising RDV-TP concentration up to 300 μM versus 28-fold for SARS-CoV-2 replicase.

T-1106-TP is incorporated via the LFC state and with a low probability

Pyrazine-carboxamide is a promising family of antiviral NA, from which the best-known member is Favipiravir (T-705), recently approved to treat influenza virus infection²⁷, and considered against SARS-CoV-2. We studied here another member of this family, T-1106 triphosphate (T-1106-TP), which is chemically more stable than T-705, while presenting similar antiviral properties^{12,20}. T-1106-TP competes for incorporation against ATP and GTP in a sequence-dependent context^{12,20}. Adding 500 μM of T-1106-TP in a reaction buffer containing 500 μM NTPs significantly increased the number and duration of pauses observed in SARS-CoV-2 replication traces (**Fig. 3a**), leading to a 2.6-fold increase in median replication time, i.e. from (25 ± 1) s to (65 ± 4) s (**Fig. 3b**). For comparison, 50 μM of RDV-TP induced

a median replication time of (72 ± 6) s at the same concentration of competing NTP, suggesting that RDV-TP is better incorporated than T-1106-TP. The final product length was not affected by T-1106-TP, supporting that T-1106-TP mechanism of action is not termination (**Fig. 3c**). Investigating how increasing T-1106-TP concentration affects SARS-CoV-2 replication kinetics (**Fig. 3d, Extended data Fig. 6**), we found that only Pause 2 exit rate was affected, decreasing by 10-fold, i.e. from (1.59 ± 0.21) s⁻¹ to (0.16 ± 0.01) s⁻¹ (**Fig. 3e**). On the other hand, Pause 1 and Pause 2 probabilities remained constant (**Extended data Fig. 3f**). Our results suggest an incorporation of T-1106-TP via the LFC state, but only on the mismatch pathway, i.e. the TMC state (**Extended data Fig. 1d**), which explains its lesser promiscuity than RDV-TP. Interestingly, the probability to enter the long-lived pause state increased by almost 5-fold, i.e. from (0.0005 ± 0.0001) to (0.0023 ± 0.0004) (**Fig. 3f**). For poliovirus RdRp, we observed that T-1106-TP incorporation induced pauses with context dependent durations²⁰, and we suggest that the incorporation of T-1106-TP in a different sequence context may result in pauses of different natures, i.e. Pause 2 and long-lived pause.

ddhCTP represents a promising NA against coronavirus infection

Finally, we have compared two chain terminators, i.e. Sofosbuvir and ddhCTP. Sofosbuvir is a uridine analog and FDA approved drug to treat hepatitis C virus infection^{28,29} and is incorporated by SARS-CoV-2 replicase^{16,19}. 3'-deoxy-3',4'-didehydro-CTP (ddhCTP) is a recently discovered natural antiviral NA produced in mammalian cells by the viperin-catalyzed conversion of CTP via a radical-based mechanism³⁰. While ddhCTP has been shown to efficiently terminate flavivirus replication both in vitro and in vivo, its antiviral activity against SARS-CoV-2 replicase remains unknown. The presence of 500 μM Sofosbuvir-TP with 500 μM NTP did not affect the replication of SARS-CoV-2 (**Fig. 4a**), while early termination events appeared in the presence of 500 μM ddhCTP (**Fig. 4b**). Supporting this visual observation, SARS-CoV-2 mean replication product length was unaffected by the presence of Sofosbuvir-TP (**Fig. 4c**), while raising the ddhCTP (**Fig. 4d**) stoichiometry against CTP up to 4 reduced the mean product length from (940 ± 13) nt to (622 ± 24) nt, showing an effective incorporation rate $\gamma_{ddhCTP,500 \mu M CTP} = (1221 \pm 130)$ nt (**Fig. 4d**). For both NAs, the replication time was unaffected (**Extended data Fig. 7a and 8a**), as well as SARS-CoV-2 replication kinetics (**Extended data Fig. 7b-d and 7f-h**). Reducing the concentration of their respective competing NTP down to 50 μM and keeping the other NTPs at 500 μM, Sofosbuvir-TP showed few early termination events when added at 500 μM (**Fig. 4e**), while only a small number of traces reached the end of the template at the same concentration of ddhCTP (**Fig.**

4f). The analysis showed a limited impact of Sofosbuvir-TP on the mean product length, i.e. with a minimum of (563 ± 32) nt at a stoichiometry of 20 (**Fig. 4g**), while ddhCTP was more effectively incorporated, shortening the mean product length down to (284 ± 23) nt at the same stoichiometry (**Fig. 4h**). Their respective effective incorporation rate at stoichiometry of 1 reflected these observations, i.e. $\gamma_{sofosbuvir,50 \mu M UTP} = (3908 \pm 467)$ nt and $\gamma_{ddhCTP,50 \mu M CTP} = (1360 \pm 71)$ nt. In other words, SARS-CoV-2 replicase incorporates in average 3908 and 1360 nt before incorporating a single Sofosbuvir-TP and ddhCTP, respectively, and terminate replication. Replication kinetics were unaffected by the presence of ddhCTP or Sofosbuvir-TP, while their median replication time mildly decreased at high stoichiometry, highlighting the shortening of the replication product (**Extended data Fig. 7a-h** and **8a-h, respectively**). As for 3'-dATP, our data suggest that stoichiometry against the competing NTP regulates Sofosbuvir-TP and ddhCTP incorporation, which are therefore incorporated via the HFC state (**Fig. 1d**). On the one hand, our data confirmed the poor incorporation of Sofosbuvir by SARS-CoV-2^{16,31}. On the other hand, ddhCTP showed an interesting increase in termination activity at physiological CTP concentration, opening great perspectives for ddhCTP as an effective anti-coronavirus NA with a low cytotoxicity.

Discussion

We present here the first observation of SARS-CoV-2 replication activity at the single molecule level. We show that SARS-CoV-2 replicase is the fastest RNA polymerase to date, replicating up to ~ 170 nt/s at 37°C. With our assay we characterized the incorporation rate and mechanism of action of several NAs, i.e. 3'-dATP, Sofosbuvir-TP, ddhCTP, T-1106-TP and RDV-TP. Here, we showed that RDV-TP is incorporated by both pathways of the LFC state, i.e. as a cognate base (diagonal arrow in **Fig. 1d**) and as a mismatch (TMC state in **Fig. 1d**). In contrast, T-1106-TP is only incorporated via the TMC state. At a saturating concentration of NTP, Pause 1 (kinetic signature of cognate base incorporation by LFC) and Pause 2 (kinetic signature of mismatch incorporation by LFC) respectively account for $\sim 6\%$ and $\sim 0.3\%$ of all the nucleotide addition events, which therefore defines an upper limit for RDV-TP and T-1106-TP relative incorporation, and explains why RDV-TP is much better incorporated than Favipiravir³¹. A recent study performed at submicromolar NTPs showed that RDV-TP is three times better incorporated than ATP¹⁶. At such low NTP concentration, the LFC state is predominant over the HFC state^{20,21}, which would suggest that the measured selectivity is only valid for the LFC state. Nonetheless, RDV-TP may still be incorporated via the HFC state, generating a long-lived pause, which would explain the observed surge in probability for this type of pause.

However, other explanations for this surge are also likely, e.g. multiple RDV-TP incorporation in a single dwell time, sequence-dependent context pause associated with RDV-TP incorporation²⁰. Importantly, we unambiguously showed that both RDV-TP and T-1106-TP are not terminators, but rather slow down replication. Concerning obligatory terminators, the effective incorporation rate we measured showed that 3'-dATP and ddhCTP are well incorporated by SARS-CoV-2 replicase, while Sofosbuvir-TP is strongly outcompeted by UTP. Interestingly, all of them are incorporated via the HFC state, i.e. behaving like a cognate base (**Fig. 1d**), supporting a mechanism where base pairing is the main discriminator by which state, i.e. HFC or LFC, is the analogue incorporated, and we are able to determine their respective effective incorporation rate. A recent steady-state kinetic study showed that nucleotide analogues modified at the 2' and 3' positions are strongly discriminated against their competing natural nucleotide¹⁶. Such selectivity is an issue for purine-based analogues which competes with high concentrations of ATP and GTP in the cell, but not for pyrimidine-based analogues, as derivatives of CTP, which compete with CTP at an intracellular concentration of ~100 μ M³². These features make ddhCTP a particularly attractive antiviral NA. Furthermore, under certain conditions, the interferon α -induced viperin converts up to 30% the cellular pool of CTP into ddhCTP, further increasing its stoichiometry and favoring its potency³⁰. This may explain why SARS-CoV-2 viral proteins inhibits the interferon response³³. ddhCTP therefore represents an exciting viral replication inhibitor with a low cytotoxicity and high efficacy. Given these insightful results, we anticipate that our assay will become the new standard to determine the selectivity and the mode of action of NAs. Future work will focus on assembling a complete coronavirus replicase, e.g. including the helicase nsp13 and the exonuclease nsp14, to evaluate their impact on SARS-CoV-2 replication, proofreading and NA efficacy.

References and notes:

- 1 Kirchdoerfer, R. N. & Ward, A. B. Structure of the SARS-CoV nsp12 polymerase bound to nsp7 and nsp8 co-factors. *Nature communications* **10**, 2342, doi:10.1038/s41467-019-10280-3 (2019).
- 2 Hillen, H. S. *et al.* Structure of replicating SARS-CoV-2 polymerase. *Nature*, doi:10.1038/s41586-020-2368-8 (2020).
- 3 Gao, Y. *et al.* Structure of the RNA-dependent RNA polymerase from COVID-19 virus. *Science (New York, N.Y)* **368**, 779-782, doi:10.1126/science.abb7498 (2020).
- 4 Wang, Q. *et al.* Structural Basis for RNA Replication by the SARS-CoV-2 Polymerase. *Cell* **182**, 417-428 e413, doi:10.1016/j.cell.2020.05.034 (2020).
- 5 Chen, J. *et al.* Structural basis for helicase-polymerase coupling in the SARS-CoV-2 replication-transcription complex. *bioRxiv*, doi:10.1101/2020.07.08.194084 (2020).

- 6 Agostini, M. L. *et al.* Coronavirus Susceptibility to the Antiviral Remdesivir (GS-5734) Is Mediated by the Viral Polymerase and the Proofreading Exoribonuclease. *Mbio* **9**, doi:10.1128/mBio.00221-18 (2018).
- 7 Bouvet, M. *et al.* RNA 3'-end mismatch excision by the severe acute respiratory syndrome coronavirus nonstructural protein nsp10/nsp14 exoribonuclease complex. *Proceedings of the National Academy of Sciences of the United States of America* **109**, 9372-9377, doi:10.1073/pnas.1201130109 (2012).
- 8 Ferron, F. *et al.* Structural and molecular basis of mismatch correction and ribavirin excision from coronavirus RNA. *Proceedings of the National Academy of Sciences of the United States of America* **115**, E162-E171, doi:10.1073/pnas.1718806115 (2018).
- 9 Ogando, N. S. *et al.* The Curious Case of the Nidovirus Exoribonuclease: Its Role in RNA Synthesis and Replication Fidelity. *Front Microbiol* **10**, 1813, doi:10.3389/fmicb.2019.01813 (2019).
- 10 Subissi, L. *et al.* One severe acute respiratory syndrome coronavirus protein complex integrates processive RNA polymerase and exonuclease activities. *Proceedings of the National Academy of Sciences of the United States of America* **111**, E3900-3909, doi:10.1073/pnas.1323705111 (2014).
- 11 Eckerle, L. D., Lu, X., Sperry, S. M., Choi, L. & Denison, M. R. High fidelity of murine hepatitis virus replication is decreased in nsp14 exoribonuclease mutants. *Journal of virology* **81**, 12135-12144, doi:10.1128/JVI.01296-07 (2007).
- 12 Shannon, A. *et al.* Favipiravir strikes the SARS-CoV-2 at its Achilles heel, the RNA polymerase. *bioRxiv*, doi:10.1101/2020.05.15.098731 (2020).
- 13 Smith, E. C., Blanc, H., Surdel, M. C., Vignuzzi, M. & Denison, M. R. Coronaviruses lacking exoribonuclease activity are susceptible to lethal mutagenesis: evidence for proofreading and potential therapeutics. *PLoS pathogens* **9**, e1003565, doi:10.1371/journal.ppat.1003565 (2013).
- 14 Siegel, D. *et al.* Discovery and Synthesis of a Phosphoramidate Prodrug of a Pyrrolo[2,1-f][triazin-4-amino] Adenine C-Nucleoside (GS-5734) for the Treatment of Ebola and Emerging Viruses. *J Med Chem* **60**, 1648-1661, doi:10.1021/acs.jmedchem.6b01594 (2017).
- 15 Gordon, C. J., Tchesnokov, E. P., Feng, J. Y., Porter, D. P. & Gotte, M. The antiviral compound remdesivir potently inhibits RNA-dependent RNA polymerase from Middle East respiratory syndrome coronavirus. *The Journal of biological chemistry* **295**, 4773-4779, doi:10.1074/jbc.AC120.013056 (2020).
- 16 Gordon, C. J. *et al.* Remdesivir is a direct-acting antiviral that inhibits RNA-dependent RNA polymerase from severe acute respiratory syndrome coronavirus 2 with high potency. *The Journal of biological chemistry* **295**, 6785-6797, doi:10.1074/jbc.RA120.013679 (2020).
- 17 Pruijssers, A. J. & Denison, M. R. Nucleoside analogues for the treatment of coronavirus infections. *Curr Opin Virol* **35**, 57-62, doi:10.1016/j.coviro.2019.04.002 (2019).
- 18 Jockusch, S. *et al.* A library of nucleotide analogues terminate RNA synthesis catalyzed by polymerases of coronaviruses that cause SARS and COVID-19. *Antiviral research* **180**, 104857, doi:10.1016/j.antiviral.2020.104857 (2020).
- 19 Chien, M. *et al.* Nucleotide Analogues as Inhibitors of SARS-CoV-2 Polymerase, a Key Drug Target for COVID-19. *J Proteome Res*, doi:10.1021/acs.jproteome.0c00392 (2020).
- 20 Dulin, D. *et al.* Signatures of Nucleotide Analog Incorporation by an RNA-Dependent RNA Polymerase Revealed Using High-Throughput Magnetic Tweezers. *Cell Rep* **21**, 1063-1076, doi:10.1016/j.celrep.2017.10.005 (2017).

- 21 Dulin, D. *et al.* Elongation-Competent Pauses Govern the Fidelity of a Viral RNA-
Dependent RNA Polymerase. *Cell Rep* **10**, 983-992, doi:10.1016/j.celrep.2015.01.031
(2015).
- 22 Seifert, M. *et al.* Temperature controlled high-throughput magnetic tweezers show
striking difference in activation energies of replicating viral RNA-dependent RNA
polymerases. *Nucleic acids research*, doi:10.1093/nar/gkaa233 (2020).
- 23 Dulin, D., Berghuis, B. A., Depken, M. & Dekker, N. H. Untangling reaction pathways
through modern approaches to high-throughput single-molecule force-spectroscopy
experiments. *Curr Opin Struct Biol* **34**, 116-122, doi:10.1016/j.sbi.2015.08.007 (2015).
- 24 Castro, C., Arnold, J. J. & Cameron, C. E. Incorporation fidelity of the viral RNA-
dependent RNA polymerase: a kinetic, thermodynamic and structural perspective. *Virus
Res* **107**, 141-149, doi:10.1016/j.virusres.2004.11.004 (2005).
- 25 Arnold, J. J. *et al.* Sensitivity of mitochondrial transcription and resistance of RNA
polymerase II dependent nuclear transcription to antiviral ribonucleosides. *PLoS
pathogens* **8**, e1003030, doi:10.1371/journal.ppat.1003030 (2012).
- 26 Pruijssers, A. J. *et al.* Remdesivir Inhibits SARS-CoV-2 in Human Lung Cells and
Chimeric SARS-CoV Expressing the SARS-CoV-2 RNA Polymerase in Mice. *Cell Rep*
32, 107940, doi:10.1016/j.celrep.2020.107940 (2020).
- 27 Furuta, Y. *et al.* T-705 (favipiravir) and related compounds: Novel broad-spectrum
inhibitors of RNA viral infections. *Antiviral research* **82**, 95-102,
doi:10.1016/j.antiviral.2009.02.198 (2009).
- 28 Kayali, Z. & Schmidt, W. N. Finally sofosbuvir: an oral anti-HCV drug with wide
performance capability. *Pharmgenomics Pers Med* **7**, 387-398,
doi:10.2147/PGPM.S52629 (2014).
- 29 Sofia, M. J. *et al.* Discovery of a beta-d-2'-deoxy-2'-alpha-fluoro-2'-beta-C-
methyluridine nucleotide prodrug (PSI-7977) for the treatment of hepatitis C virus. *J
Med Chem* **53**, 7202-7218, doi:10.1021/jm100863x (2010).
- 30 Gizzi, A. S. *et al.* A naturally occurring antiviral ribonucleotide encoded by the human
genome. *Nature* **558**, 610-614, doi:10.1038/s41586-018-0238-4 (2018).
- 31 Xie, X. *et al.* A nanoluciferase SARS-CoV-2 for rapid neutralization testing and
screening of anti-infective drugs for COVID-19. *bioRxiv*,
doi:10.1101/2020.06.22.165712 (2020).
- 32 Traut, T. W. Physiological concentrations of purines and pyrimidines. *Molecular and
cellular biochemistry* **140**, 1-22, doi:10.1007/BF00928361 (1994).
- 33 Sa Ribero, M., Jouvenet, N., Dreux, M. & Nisole, S. Interplay between SARS-CoV-2
and the type I interferon response. *PLoS pathogens* **16**, e1008737,
doi:10.1371/journal.ppat.1008737 (2020).
- 34 Ostrofet, E., Papini, F. S. & Dulin, D. Correction-free force calibration for magnetic
tweezers experiments. *Sci Rep* **8**, 15920, doi:10.1038/s41598-018-34360-4 (2018).
- 35 Papini, F. S., Seifert, M. & Dulin, D. High-yield fabrication of DNA and RNA
constructs for single molecule force and torque spectroscopy experiments. *Nucleic acids
research*, doi:10.1093/nar/gkz851 (2019).
- 36 Cnossen, J. P., Dulin, D. & Dekker, N. H. An optimized software framework for real-
time, high-throughput tracking of spherical beads. *The Review of scientific instruments*
85, 103712, doi:10.1063/1.4898178 (2014).
- 37 Cowan, G. *Statistical Data Analysis*. (Oxford University Press, 1998).
- 38 Press, W. H., Flannery, B. P., Teukolsky, S. A. & Vetterling, W. T. *NUMERICAL
RECIPES IN C: THE ART OF SCIENTIFIC COMPUTING*. (Cambridge University
Press, 1992).

Author contribution: DD and CEC conceived the research. MS, SCB and DD performed and analyzed the single molecule experiments. PvN wrote the MLE analysis routine. MD derived the terminator competition model. TG and SCA provided ddhCTP. BC, TTNL and AS provided SARS-CoV-1 proteins. RNK provided SARS-CoV-2 proteins. DD and CEC wrote the article. All the authors have discussed the data and edited the article.

Acknowledgements: We thank Joy Feng from Gilead Sciences to provide RDV-TP, and Veronique Fattorini and Barbara Selisko for excellent technical assistance and help in the experiments. DD was supported by the Interdisciplinary Center for Clinical Research (IZKF) at the University Hospital of the University of Erlangen-Nuremberg. RNK was supported by the National Institutes of Health, National Institute for Allergy and Infectious Disease (AI123498). AS, TTNL and BC acknowledge grants by the Fondation pour la Recherche Médicale (Aide aux équipes), the SCORE project H2020 SC1-PHE-Coronavirus-2020 (grant#101003627), and the REACTing initiative (REsearch and ACTION targeting emerging infectious diseases).

Competing interests: Authors declare no competing interest

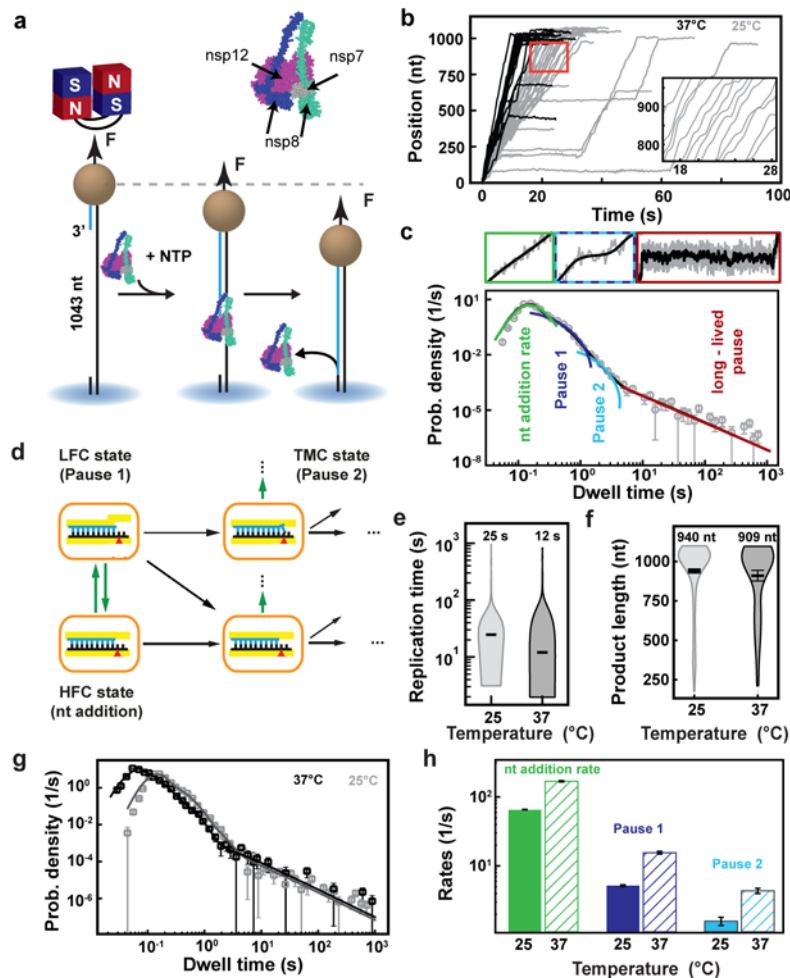


Fig. 1. SARS-CoV-2 replicase is a fast and processive viral replication complex. **a**, Schematic of magnetic tweezers assay to monitor RNA synthesis by the SARS-CoV-2 replicase complex. A magnetic bead is attached to a glass coverslip surface by a 1043 long ssRNA construct that experiences a constant force F . The replicase formed by nsp7, nsp8 and nsp12 assembles at the 3'-end of the RNA strand annealed to the template. The subsequent conversion of the ssRNA template into dsRNA reduces the end-to-end extension of the tether, signaling replication activity. **b**, SARS-CoV-2 replication traces acquired at either 25°C (gray) or 37°C (black), showing bursts of nucleotide addition interrupted by pauses. The inset is a zoom-in of the traces captured in the red square. **c**, The dwell times collected from (b) are assembled into a distribution that is fitted using a pause-stochastic model (**Materials and Methods**) (solid lines). The model includes four different probability distribution functions that describe the event that kinetically dominates the dwell time: uninterrupted ten nucleotide additions (green); exponentially distributed Pause 1 and 2 (blue and cyan, respectively); and the power law distributed long-lived pauses (red). **d**, The dwell time distribution in (c) is described by the viral RdRp kinetic model (adapted from Ref. ²¹). Nucleotide addition is achieved via two competing pathways, i.e. the high fidelity catalytic (HFC) state and the low fidelity catalytic (LFC) state, which leads to either cognate, i.e. diagonal arrow, or non cognate nucleotide incorporation, i.e. terminal mismatch catalytic (TMC). The former dominates at high NTP concentration, is fast and accurate, while the latter dominates at low NTP concentration, is slow and error prone. Pause 1 and Pause 2 are the kinetic signature of cognate and mismatch nucleotide additions, respectively, by the LFC state. **e**, Total replication time and **f**, replication product length of SARS-CoV-2 replication activity at either 25°C or 37°C. The median total replication time and mean product length are indicated above the violin plots, and represented as thick horizontal lines. The error bars represent one standard deviation extracted from 1000 bootstraps. **g**, Dwell

time distributions of SARS-CoV-2 replication activity at 25°C (grey circles) and 37°C (black circles) extracted from (b), and their respective fit to the pause-stochastic model (corresponding solid lines). **h**, Nucleotide addition rate (green), Pause 1 (dark blue) and Pause 2 (cyan) exit rates at either 25°C or 37°C (solid and hatched bars, respectively) extracted from (g). The error bars in (c) and (g) are 36% confidence interval extracted from 1000 bootstraps. The error bars in (h) are one standard deviation extracted from 100 bootstraps (**Materials and Methods**).

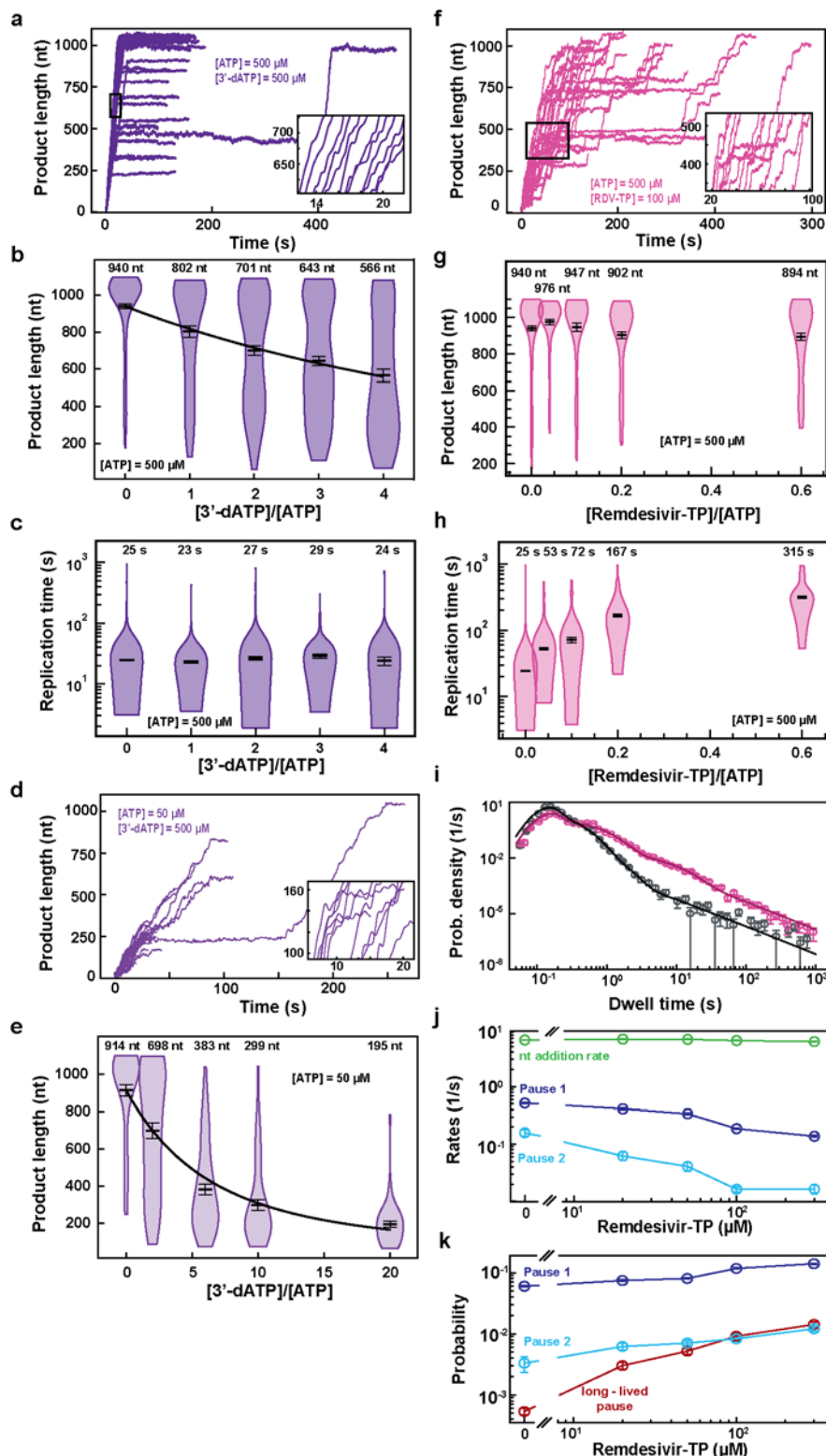


Fig. 2. Remdesivir-TP (RDV-TP) is efficiently incorporated and dramatically increases the average replication time. **a**, SARS-CoV-2 replication traces for 500 μM NTPs and 500 μM 3'-dATP; and **f**, for 500 μM NTPs and 100 μM RDV-TP. **b**, **g**, **e**, SARS-CoV-2 replication product length for the 1043 nt long template using the indicated concentration of ATP, 500 μM of other NTPs, as a function of the stoichiometry of either [3'-dATP]/[ATP] or [RDV-TP]/[ATP]. The mean values are indicated above the violin plots, and represented by horizontal black thick lines flanked by one standard deviation error bars extracted from 1000 bootstraps. **c**, **h**, Replication time for the reaction conditions described in (b, g). The medians are indicated above the violin plots, and represented by horizontal black thick lines flanked by one standard

deviation error bars extracted from 1000 bootstraps. **i**, Dwell time distributions of SARS-CoV-2 replication activity for 500 μM NTPs in the absence (gray) or presence of 100 μM RDV-TP (pink). The corresponding solid lines are the fit of the pause-stochastic model. **j**, Nucleotide addition rate (green), Pause 1 (dark blue) and Pause 2 (cyan) exit rates for $[\text{NTPs}] = 500 \mu\text{M}$ and several $[\text{RDV-TP}]$. **k**, Probabilities to enter Pause 1 (dark blue), Pause 2 (cyan) and the power law (red) distributed states for the conditions described in (j). In (b, e), the solid lines are the fits of the terminator effective incorporation rate (**Materials and Methods**). In (a, d, g), the insets are zoom-in of the replication traces captured in the black square. Error bars in (i) are the 36% CI from extracted from 1000 bootstraps. Error bars in (j, k) are one standard deviation extracted from 100 bootstrap procedures (**Materials and Methods**).

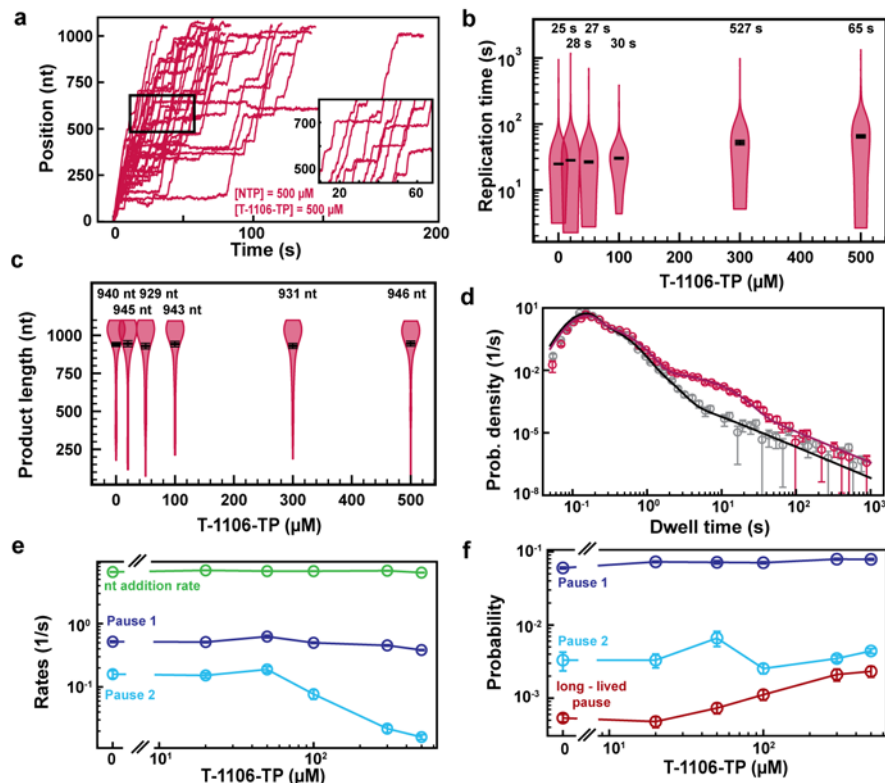


Fig. 3. T-1106-TP incorporation induces intermediate duration pauses in SARS-CoV-2 replication kinetics. **a**, SARS-CoV-2 replication traces in the presence of 500 μM NTPs, in the presence of 500 μM T-1106-TP. The inset is a zoom-in of the replication traces captured in the black square. **b**, SARS-CoV-2 replication time for the 1043 nt long template using 500 μM of all NTPs, and the indicated concentration of T-1106-TP. The median values are indicated above the violin plots, and represented by horizontal black thick lines flanked by one standard deviation error bars extracted from 1000 bootstraps. **c**, Replication product length using 500 μM NTPs and the indicated concentration of T-1106-TP. The mean values are indicated above the violin plots, and represented by horizontal black thick lines flanked by one standard deviation error bars extracted from 1000 bootstraps. **d**, Dwell time distributions of SARS-CoV-2 replication activity for 500 μM NTP either without (gray) or with 500 μM (red) T-1106-TP. The corresponding solid lines are the fit to the pause-stochastic model. **e**, Nucleotide addition rate (green), Pause 1 (dark blue) and Pause 2 (cyan) exit rates for [NTPs] = 500 μM and several T-1106-TP concentrations. **f**, Probabilities to enter Pause 1 (dark blue), Pause 2 (cyan) and the power law (red) distributed states for the conditions described in (e). The error bars denote the 36% CI from 1000 bootstraps in (d). Error bars in (e, f) are one standard deviation extracted from 100 bootstrap procedures (**Materials and Methods**).

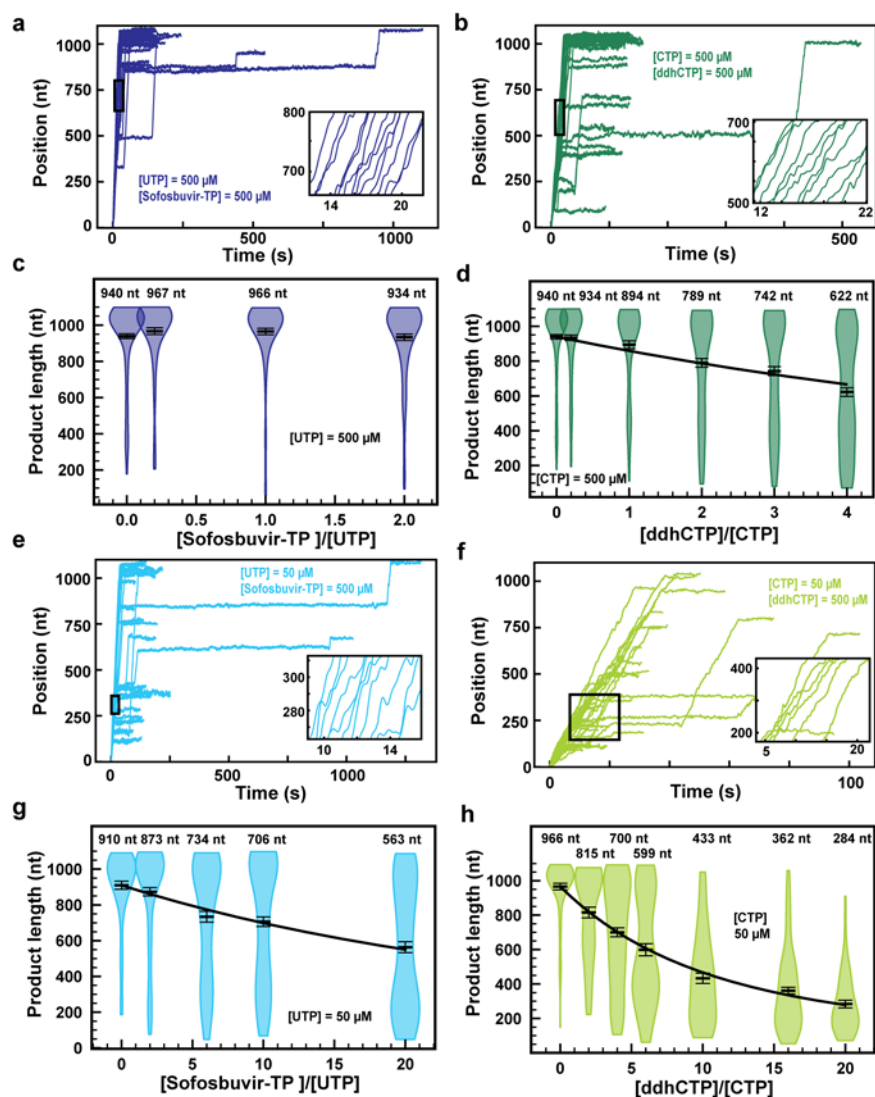


Fig. 4. ddhCTP is a potent inhibitor of SARS-CoV-2 replication, Sofosbuvir-TP isn't. **a, b,** SARS-CoV-2 replication traces for 500 μM NTPs and 500 μM of either Sofosbuvir-TP or ddhCTP. **c, d,** SARS-CoV-2 replication product length using the indicated concentration of either UTP or CTP, 500 μM of other NTPs, as a function of the stoichiometry of either (b) [Sofosbuvir-TP]/[UTP] or (c) [ddhCTP]/[CTP]. The mean values are indicated above the violin plots, and represented by horizontal black thick lines flanked by one standard deviation error bars extracted from 1000 bootstraps. **e, f,** SARS-CoV-2 replication traces in the presence 50 μM of either (e) UTP or (f) CTP, 500 μM of all other NTPs and 500 μM of either (e) Sofosbuvir-TP or (f) ddhCTP. **g, h,** SARS-CoV-2 replication product length using 50 μM either UTP or CTP, 500 μM of other NTPs, as a function of the stoichiometry of either (g) [Sofosbuvir-TP]/[UTP] or (h) [ddhCTP]/[CTP]. The mean values are indicated above the violin plots, and represented by horizontal black thick lines flanked by one standard deviation error bars extracted from 1000 bootstraps. In (f, d, h), the solid lines are the fits of the terminator effective incorporation rate (**Materials and Methods**). In (a, b, e, f), the insets are a zoom-in of the replication traces captured in the black square.

Materials and methods

High throughput magnetic tweezers apparatus

The high throughput magnetic tweezers used in this study have been described in detail elsewhere³⁴. Shortly, a pair of vertically aligned permanent magnets (5 mm cubes, SuperMagnete, Switzerland) separated by a 1 mm gap are positioned above a flow cell (see paragraph below) that is mounted on a custom-built inverted microscope. The vertical position and rotation of the magnets are controlled by two linear motors, M-126-PD1 and C-150 (Physik Instrumente PI, GmbH & Co. KG, Karlsruhe, Germany), respectively. The field of view is illuminated through the magnets gap by a collimated LED-light source, and is imaged onto a large chip CMOS camera (Dalsa Falcon2 FA-80-12M1H, Stemmer Imaging, Germany) using a 50× oil immersion objective (CFI Plan Achrom 50 XH, NA 0.9, Nikon, Germany) and an achromatic doublet tube lens of 200 mm focal length and 50 mm diameter (Qioptic, Germany). To control the temperature, we used a system described in details in Ref.²². Shortly, a flexible resistive foil heater with an integrated 10MΩ thermistor (HT10K, Thorlabs) is wrapped around the microscope objective and further insulated by several layers of kapton tape (KAP22-075, Thorlabs). The heating foil is connected to a PID temperature controller (TC200 PID controller, Thorlabs) to adjust the temperature within ~0.1°.

Recombinant Protein Expression of RdRp (nsp12) and cofactors (nsp7 and nsp8) from SARS-CoV-2

This protocol was described in Ref.¹⁹. SARS-CoV-2 nsp12: The SARS-CoV-2 nsp12 gene was codon optimized and cloned into *pFastBac* with C-terminal additions of a TEV site and strep tag (Genscript). The *pFastBac* plasmid and DH10Bac *E. coli* (Life Technologies) were used to create recombinant bacmids. The bacmid was transfected into Sf9 cells (Expression Systems) with Cellfectin II (Life Technologies) to generate recombinant baculovirus. The baculovirus was amplified through two passages in Sf9 cells, and then used to infect 1 L of Sf21 cells (Expression Systems) and incubated for 48 hrs at 27°C. Cells were harvested by centrifugation, resuspended in wash buffer (25 mM HEPES pH 7.4, 300 mM NaCl, 1 mM MgCl₂, 5 mM DTT) with 143 μl of BioLock per liter of culture. Cells were lysed via microfluidization (Microfluidics). Lysates were cleared by centrifugation and filtration. The protein was purified using Strep Tactin superflow agarose (IBA). Strep Tactin eluted protein was further purified by size exclusion chromatography using a Superdex 200 Increase 10/300 column (GE Life Sciences) in 25 mM HEPES, 300 mM NaCl, 100 μM MgCl₂, 2 mM TCEP, at pH 7.4. Pure protein was concentrated by ultrafiltration prior to flash freezing in liquid nitrogen. SARS-CoV-2 *nsp7* and *nsp8*: The SARS-CoV-2 *nsp7* and *nsp8* genes were codon optimized and cloned into pET46 (Novagen) with an N-terminal 6x histidine tag, an enterokinase site, and a TEV protease site. Rosetta2 pLys *E. coli* cells (Novagen) were used for bacterial expression. After induction with isopropyl β-D-1-thiogalactopyranoside (IPTG), cultures were grown at 16°C for 16 hrs. Cells were harvested by centrifugation and pellets were resuspended in wash buffer (10 mM Tris pH 8.0, 300 mM NaCl, 30 mM imidazole, 2 mM DTT). Cells were lysed via microfluidization and lysates were cleared by centrifugation and filtration. Proteins were purified using Ni-NTA agarose beads and eluted with wash buffer containing 300 mM imidazole. Eluted proteins were further purified by size exclusion chromatography using a Superdex 200 Increase 10/300 column (GE Life Sciences). Purified proteins were concentrated by ultrafiltration prior to flash freezing with liquid nitrogen.

Recombinant Protein Expression of RdRp (nsp12) and cofactors (nsp7 and nsp8) from SARS-CoV-1

This protocol was described in Ref.¹². All SARS-CoV proteins used in this study were expressed in *Escherichia coli* (*E. coli*), under the control of T5 promoters. Cofactors *nsp7L8* and *nsp8* alone were expressed from pQE30 vectors with C-terminal and N-terminal hexa-

histidine tags respectively. TEV cleavage site sequences were included for His-tag removal following expression. The nsp7L8 fusion protein was generated by inserting a GSGSGS linker between nsp7- and nsp8-coding sequences. Cofactors were expressed in NEB Express C2523 (New England Biolabs) cells carrying the pRare2LacI (Novagen) plasmid in the presence of Ampicillin (100 μ M/mL) and Chloramphenicol (17 μ g/mL). Protein expression was induced with 100 μ M IPTG once the OD600 = 0.5–0.6, and expressed overnight at 17°C. Protein was purified first through affinity chromatography with HisPur Cobalt resin (Thermo Scientific), with a lysis buffer containing 50 mM Tris-HCl pH 8, 300 mM NaCl, 10 mM Imidazole, supplemented with 20 mM MgSO₄, 0.25 mg/mL Lysozyme, 10 μ g/mL DNase, 1 mM PMSF, with lysis buffer supplemented with 250 mM imidazole. Eluted protein was concentrated and dialyzed overnight in the presence of histidine labeled TEV protease (1:10 w/w ratio to TEV:protein) for removal of the protein tag. Cleaved protein was purified through a second cobalt column and protein was purified through size exclusion chromatography (GE, Superdex S200) in gel filtration buffer (25 mM HEPES pH 8, 150 mM NaCl, 5mM MgCl₂, 5 mM TCEP). Concentrated aliquots of protein were flash-frozen in liquid nitrogen and stored at -80 °C. A synthetic, codon-optimized SARS-CoV nsp12 gene (DNA 2.0) bearing C-terminal 8His-tag preceded by a TEV protease cleavage site was expressed from a pJ404 vector (DNA 2.0) in E. coli strain BL21/pG-Tf2 (Takara). Cells were grown at 37°C in the presence of Ampicillin and Chloramphenicol until OD600 reached 2. Cultures were induced with 250 μ M IPTG and protein expressed at 17°C overnight. Purification was performed as above in lysis buffer supplemented with 1% CHAPS. Two additional wash steps were performed prior to elution, with buffer supplemented with 20 mM imidazole and 50 mM arginine for the first and second washes respectively. Polymerase was eluted using lysis buffer with 500 mM imidazole and concentrated protein was purified through gel filtration chromatography (GE, Superdex S200) in the same buffer as for nsp7L8. Collected fractions were concentrated and supplemented with 50% glycerol final concentration and stored at -20 °C.

Construct fabrication.

The fabrication of the RNA hairpin has been described in detail in Ref. ³⁵. The RNA hairpin is made of a 499 bp double-stranded RNA stem terminated by a 20 nt loop that is assembled from three ssRNA annealed together (**Extended data Fig. 1a**), and two handles, one of 856 bp at the 5' end and one 822 bp at the 3' end. The handles include either an 343 nt digoxigenin-labeled ssRNA or an 443 nt biotin-labeled ssRNA (**Extended data Fig. 1a**). Upon applied force above ~21 pN, the hairpin opens and frees a 1043 nt ssRNA template for SARS-CoV-2 replication (**Extended data Fig. 1b**). To obtain the different parts of the RNA construct, template DNA fragments were amplified via PCR, purified (Monarch PCR and DNA cleanup kit) and in vitro transcribed (NEB HiScribe™ T7 High Yield RNA Synthesis Kit). Transcripts were then treated with Antarctic Phosphatase and T4 Polynucleotide Kinase. RNAs were purified using the RNA Clean & Concentrator-25 kit (Zymo Research). Individual RNA fragments were annealed and ligated with T4 RNA ligase 2 (NEB) to assemble the RNA hairpin.

DNA sequence encoding the RNA used as template by SARS-CoV-2 (highlighted in yellow and in grey are the loop and the ssRNA template preceding the hairpin stem where the replicase loads, respectively)

```
GTTCTACATAGCGTGCAGACGTGAATTTAATCTCGCTGACGTGTAGACACAGTGC
GTCTGCTGTCGGGTCCCTCTGGTGACTGGGTAGTTGGACTTGCCCTTGGAAGACA
TAGCAAGACCCTGCCTCTCTATTGATGTCACGGCGAATGTCGGGGAGACAGCAGC
GGCTGCAGACATCAGATCGGAGTAATACTCTCCGTA ACTGGCCTTCTCTGAATTC
CGACGTTGTTAAGATGGCAGAGCCCGGTAATCGCTACTTGACCAGATAAGCTTTC
CGTGGATGGTTTAGAGGAATCACATCCAAGACTGGCTAAGCACGAAGCAACTCTT
GAGTGTA AAATTGTTGTCTCTCTGTATTCGGGATGCGGGTACTAGATGACTGCAGG
```

GACTCCGACGTTAAGTACATTACCCCGTCATAGGGCGCCGTTTCAGGATCACGTTAC
CGCCATAAGATGGGAGCATGACTTCTTCTCCGCTGCGCCCACGGATCCAGTAGTG
ATTAACATTCGACAGCATGCGCACAATCACTACTGGATCCGTGGGCGCAGCGGA
GAAGAAGTCATGCTCCCATCTTATGGCGGTAACGTGATCCTGAACGGCGCCTATG
ACGGGGTAATGTACTTAACGTCCGAGTCCCTGCAGTCATCTAGTACCCGCATCCC
GAATACAGGAGACAACAATTTTACACTCAAGAGTTGCTTCGTGCTTAGCCAGTCT
TGGATGTGATTCTCTAAACCATCCACGGAAAGCTTATCTGGTCAAGTAGCGATT
ACCGGGCTCTGCCATCTTAACAACGTCCGGAATTCAGAGAAGGCCAGTTACGGAG
AGTATTACTCCGATCTGATGTCTGCAGCCGCTGCTGTCTCCCCGACATTCGCCGTG
ACATCAATAGAGAGGCAGGGTCTTGCTATGTCTTCCAAGGGCAAGTCCAACCTACC
CAGTCACCAGAGGGACCCGACAGCAGACGCACTGTGTCTACACGTCAGCGAGAT
TAAATTCACGTCTGCACGCTATGTAGAACCCTCAGCCAACCTCGGTCGCGTCGGA

The resulting RNA template contains 250 U (24%), 253 A (24%), 273 C (26%) and 267 G (26%).

Flow cell assembly

The fabrication procedure for flow cells has been described in details in Ref. ³⁴. To summarize, we sandwiched a double layer of Parafilm by two #1 coverslips, the top one having one hole at each end serving as inlet and outlet, the bottom one being coated with a 0.01% m/V nitrocellulose in amyl acetate solution. The flow cell is mounted into a custom-built holder and rinsed with ~1 ml of 1x phosphate buffered saline (PBS). 3 μ m diameter polystyrene reference beads are attached to the bottom coverslip surface by incubating 100 μ l of a 1:1000 dilution in PBS of (LB30, Sigma Aldrich, stock conc.: 1.828×10^{11} particles per milliliter) for ~3 minutes. The tethering of the magnetic beads by the RNA hairpin construct relies on a digoxigenin/anti-digoxigenin and biotin-streptavidin attachment at the coverslip surface and the magnetic bead, respectively. Therefore, following a thorough rinsing of the flow cell with PBS, 50 μ l of anti-digoxigenin (50 μ g/ml in PBS) is incubated for 30 minutes. The flow cell was flushed with 1 ml of 10 mM Tris, 1 mM EDTA pH 8.0, 750 mM NaCl, 2 mM sodium azide buffer to remove excess of anti-digoxigenin followed by rinsing with another 0.5 ml of 1x TE buffer (10 mM Tris, 1 mM EDTA pH 8.0 supplemented with 150 mM NaCl, 2 mM sodium azide). The surface is then passivated by incubating bovine serum albumin (BSA, New England Biolabs, 10 mg/ml in PBS and 50% glycerol) for 30 minutes, and rinsed with 1x TE buffer.

Single molecule RdRp replication activity experiments

20 μ l of streptavidin coated Dynal Dynabeads M-270 streptavidin coated magnetic beads (ThermoFisher) was mixed with ~0.1 ng of RNA hairpin (total volume 40 μ l) and incubated for ~5 minutes before rinsing with ~2 ml of 1x TE buffer to remove any unbound RNA and the magnetic beads in excess. RNA tethers were sorted for functional hairpins by looking for the characteristic jump in extension length due to the sudden opening of the hairpin during a force ramp experiment ³⁵ (**Extended data Fig. 1b**). The flow cell was subsequently rinsed with 0.5 ml reaction buffer (50 mM HEPES pH 7.9, 2 mM DTT, 2 μ M EDTA, 5 mM MgCl₂). After starting the data acquisition at a force that would keep the hairpin open, 100 μ l of reaction buffer containing either 0.6 μ M of nsp12, 1.8 μ M of nsp7 and nsp8 for SARS-CoV-2 experiments or 0.1 μ M of nsp12, 1 μ M of nsp7 and nsp8 for SARS-CoV-1 experiments, the indicated concentration of NTPs and of nucleotide analogues (if required) were flushed in the flow cell to start the reaction. Sofosbuvir-TP and T-1106-TP were purchased from Jena Bioscience (Jena, Germany) and 3'-dATP was purchased from TriLink Biotechnologies (San Diego, CA, USA). The experiments were conducted at a constant force of 35 pN for a duration of 20 to 40 minutes. The camera frame rate was fixed at either 58 Hz or 200 Hz, for reaction temperature set at either 25°C or 37°C, respectively. A custom written Labview routine ³⁶

controlled the data acquisition and the (x-, y-, z-) positions analysis/tracking of both the magnetic and reference beads in real-time. Mechanical drift correction was performed by subtracting the reference bead position to the magnetic beads positions.

Data processing

The replication activity of SARS-CoV-2 core replicase converts the tether from ssRNA to dsRNA, which concomitantly decreases the end-to-end extension of the tether. The change in extension measured in micron was subsequently converted into replicated nucleotides N_R using the following equation:

$$N_R(F) = N \cdot \frac{L_{ss}(F) - L_{meas}(F)}{L_{ss}(F) - L_{ds}(F)}$$

Where, $L_{meas}(F)$, $L_{ss}(F)$ and $L_{ds}(F)$ are the measured extension during the experiment, the extension of a ssRNA and of a dsRNA construct, respectively, experiencing a force F , and N the number of nucleotides of the ssRNA template²¹. The traces were then filtered using a Kaiser-Bessel low-pass filter with a cut-off frequency at 2 Hz. As previously described in Ref.²¹, a dwell time analysis was performed by scanning the filtered traces with non-overlapping windows of 10 nt to measure the time (coined throughout the manuscript dwell time) for SARS-CoV-2 replicase to incorporate ten successive nucleotides. The dwell times of all the traces for a given experimental condition were assembled and further analyzed using a maximum likelihood estimation (MLE) fitting routine to extract the parameters from the stochastic-pausing model (see below).

SARS-CoV-2 replication product length analysis

To extract the product length of the replication complex, only the traces where the beginning and the end could clearly be distinguished and for which the tether did not rupture for ten minutes following the last observed replication activity were considered. We represented the mean product length, as well as one standard deviation of the mean from 1000 bootstraps as error bars.

Stochastic-pausing model

The model is described in detail in²⁰⁻²². There are many kinetic models that are consistent with the empirical dwell-time distributions we observe, and we here work under the assumption that the probability of pausing is low enough that there is only one rate-limiting pause in each dwell-time window. This assumption washes out most details of the kinetic scheme that connects pauses and nucleotide addition, but allows us to determine the general form of the dwell-time distribution without specifying how the pauses are connected to the nucleotide addition pathway

$$p_{dw}(t) \propto p_{na} \Gamma\left(t; N_{dw}, \frac{1}{k_{na}}\right) + Q(t) \left(\sum_{n=1}^{N_{sp}} p_n k_n e^{-k_n t} + \frac{a_{bt}}{2(1 + t/1s)^{3/2}} \right). \quad (\text{Eq. 1})$$

In the above expression, the gamma function in the first term contributes the portion p_{na} of dwell-times that originate in the RdRp crossing the dwell-time window of size N_{dw} base pairs without pausing; the second term is a sum of contributions originating in pause-dominated transitions, each contributing a fraction p_n of dwell-times; the third term captures the asymptotic power-law decay (amplitude a_{bt}) of the probability of dwell-times dominated by a backtrack. The backtracked asymptotic term needs to be regularized for times shorter than the

diffusive backtrack step. We have introduced a regularization at 1 s, but the precise timescale does not matter, as long as it is set within the region where the exponential pauses dominate over the backtrack. From left to right, each term of Equation 1 is dominating the distribution for successively longer dwell-times.

A cut-off factor $Q(t)$ for short times is introduced to account for the fact that the dwell-time window includes N_{dw} nucleotide-addition steps,

$$Q(t) = \frac{(tk_{na}/N_{dw})^{N_{dw}-1}}{1 + (tk_{na}/N_{dw})^{N_{dw}-1}}.$$

The fit results dependence on these cut-offs is negligible as long as they are introduced in regions where the corresponding term is sub-dominant. Here the cut is placed under the center of the elongation peak, guaranteeing that it is placed where pausing is sub-dominant.

Maximum likelihood estimation. The normalized version of Equation 1 is the dwell-time distribution fit to the experimentally collected dwell-times $\{t_i\}_i$ by minimizing the likelihood function³⁷

$$L = -\sum_i \ln p_{dw}(t_i) \quad (\text{Eq. } 2)$$

with respect to rates and probabilistic weights.

Dominating in a dwell-time window vs. dominating in one step. The fractions p_n represent the probability that a particular rate k_n dominates the dwell-time. We want to relate this to the probability P_n that a specific exit rate dominates within a one-nt transcription window. Assuming we have labelled the pauses so that $k_{n-1} > k_n$, we can relate the probability of having rate n dominating in N_{dw} steps to the probability of having it dominate in one step through

$$p_n = \left(\sum_{m=0}^n P_m \right)^{N_{dw}} - \left(\sum_{m=0}^{n-1} P_m \right)^{N_{dw}}, \quad p_0 = p_{na} = P_{na}^{N_{dw}} = P_0^{N_{dw}} \quad (\text{Eq. } 3)$$

The first term in Equation 3 represents the probability of having no pauses longer than the n^{th} pause in the dwell-time window, and the second term represents the probability of having no pauses longer than the $(n-1)^{\text{th}}$ pause. The difference between the two terms is the probability that the n^{th} pause will dominate. This can be inverted to yield a relation between the single-step probabilities (P_n) and the dwell-time window probabilities (p_n)

$$P_n = \left(\sum_{m=0}^n p_m \right)^{1/N_{dw}} - \left(\sum_{m=0}^{n-1} p_m \right)^{1/N_{dw}}, \quad P_0 = p_0^{1/N_{dw}}$$

This relationship has been used throughout the manuscript to relate our fits over a dwell-time window to the single-step probabilities.

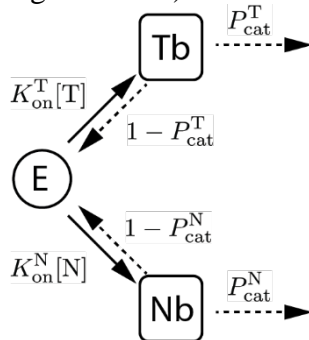
Maximum likelihood estimation (MLE) fitting routine

The above stochastic-pausing model was fit to the dwell time distributions using a custom Python 3.7 routine. Shortly, we implemented a combination of simulated annealing and bound constrained minimization to find the parameters that minimize Equation 2. We calculated the statistical error on the parameters by applying the MLE fitting procedure on 100 bootstraps of the original data set³⁸, and reported the standard deviation for each fitting parameters.

Competition between obligatory terminator nucleotide analogues and their natural nucleotide homologues

Starting with an empty active site (E), we assume that there is direct binding competition between the natural nucleotide (N) and the nucleotide analogue terminator (T, simply coined terminator) that result in either the former bound (Nb) or the latter bound (Tb) to the active site.

From these states there can be any number of intermediate states before the base is either added to the chain with probability $P_{\text{cat}}^{\text{T/N}}$, or unbinds from the pocket with probability $1 - P_{\text{cat}}^{\text{T/N}}$ (see figure below).



From the empty active site state (E), either a terminator (T) or a natural nucleotide (N) can bind though direct competition with the first order binding rates $K_{\text{on}}^{\text{T}}[\text{T}]$ and $K_{\text{on}}^{\text{N}}[\text{N}]$ (solid arrows represent rates) respectively. From the bound states (Tb/Nb) there can be many sub steps before either incorporating the base with probability $P_{\text{cat}}^{\text{T/N}}$, or ejecting it from the active site with probability $1 - P_{\text{cat}}^{\text{T/N}}$ (dashed arrows represent probabilities).

The effective incorporation rate is the attempt rate times the probability of success,

$$k_{\text{inc}}^{\text{T/N}} = [\text{T/N}] K_{\text{on}}^{\text{T/N}} P_{\text{cat}}^{\text{T/N}}$$

and the relative probability that next incorporated base is a terminator or natural nucleotide is given by the relative effective addition rates

$$\frac{p^{\text{T}}}{p^{\text{N}}} = \frac{k_{\text{inc}}^{\text{T}}}{k_{\text{inc}}^{\text{N}}} = \frac{[\text{T}] K_{\text{on}}^{\text{T}} P_{\text{cat}}^{\text{T}}}{[\text{N}] K_{\text{on}}^{\text{N}} P_{\text{cat}}^{\text{N}}}, \quad p^{\text{T}} + p^{\text{N}} = 1.$$

This can be rewritten as

$$p^{\text{N}} = \frac{\gamma}{\gamma + x}, \quad p^{\text{T}} = \frac{x}{\gamma + x}, \quad x = \frac{[\text{T}]}{[\text{N}]}, \quad \gamma = \frac{K_{\text{on}}^{\text{N}} P_{\text{cat}}^{\text{N}}}{K_{\text{on}}^{\text{T}} P_{\text{cat}}^{\text{T}}}$$

In the above x is the relative stoichiometry between T and N, while γ is the relative effective incorporation rates of N and T at equimolar conditions.

On an infinite construct, polymerization will proceed until the first T is incorporated, after which it terminates. At termination, the product has incorporated $n - 1$ Ns, and finally one T, with probability

$$P(n) = (p^{\text{N}})^{n-1} p^{\text{T}} = (1 - p^{\text{T}})^{n-1} p^{\text{T}}.$$

The average number of Ns and Ts incorporated on an infinite construct is therefore

$$n^{\infty} = \sum_{n=1}^{\infty} n (p^{\text{N}})^{n-1} p^{\text{T}} = 1/p^{\text{T}}.$$

If the construct only allows for the addition of N Ns and Ts, the average number of Ns and Ts in the product will instead be

$$n^N = \sum_{n=1}^N n_{\text{A}} (p^{\text{N}})^{n-1} p^{\text{T}} + \sum_{n=N+1}^{\infty} N (p^{\text{N}})^{n-1} p^{\text{T}} = \frac{1 - (p^{\text{N}})^N}{p^{\text{T}}} = n^{\infty} (1 - (p^{\text{N}})^N).$$

For a genome of length L , with the relative abundance q of templating bases for N and T, we thus expect there to be at most $N = qL$ Ns and Ts incorporated at termination. At termination the product then has the average length

$$l^L = \frac{n^{qL}}{q} = \frac{1 - (p^{\text{N}})^{qL}}{q p^{\text{T}}} = l^{\infty} (1 - (p^{\text{N}})^{qL}), \quad l^{\infty} = \frac{1}{q p^{\text{T}}}$$

Data fitting

Though the constructs are 1043 nucleotides long, this length is not always reached even when there are no terminators in the buffer. The average product length is about 10% shorter than the full construct length. To account for this reduction in maximal average product length, we simply fix L to be the mean product length reached without terminator in the buffer, and fit out γ from a least square fit, weighted with the inverse experimental variance.